Single and Multiple-Band Bandpass Filters Using Bandstop Resonator Sections

Lin, Jing Yu; Wong, Sai Wai; Qian, Lu; Wang, Yi; Yang, Yang; Liu, Qing Huo

DOI:
10.1109/JMW.2023.3346399

IEEE Journal of Microwaves

MTT-S MHz to THz Community

Received 11 September 2023; revised 5 December 2023; accepted 18 December 2023. Date of publication 11 January 2024; date of current version 9 April 2024.

Digital Object Identifier 10.1109/JMW.2023.3346399

Single and Multiple-Band Bandpass Filters Using Bandstop Resonator Sections

JING-YU LIN [1] (Member, IEEE), SAI-WAI WONG [2] (Senior Member, IEEE), LU QIAN [3] (Graduate Student Member, IEEE), YI WANG [3] (Senior Member, IEEE), YANG YANG [4] (Senior Member, IEEE), AND QING-HUO LIU [5,6] (Fellow, IEEE)

(Regular Paper)

[1]Institute of Electromagnetics and Acoustics, Xiamen University, Xiamen 361005, China
[2]College of Information Engineering, Shenzhen University, Shenzhen 518060, China
[3]EDT Laboratory, School of Engineering, University of Birmingham, B15 2TT Birmingham, U.K.
[4]School of Electrical and Data Engineering, University of Technology Sydney, Ultimo, NSW 2007, Australia
[5]Institute for Advanced Study, Ningbo 315200, China
[6]Xiamen University, Xiamen 361005, China

CORRESPONDING AUTHOR: Sai-Wai Wong (e-mail: wongsaiwai@ieee.org).

This work was supported in part by the National Natural Science Foundation of China under Grant 62171289; in part by the Australian Research Council under Grant LP210300004; and in part by the Shenzhen Science and Technology Programs under Grant JCYJ 20190728151457763.

ABSTRACT In this paper, the design methodology and implementation of single-band and multiple-band elliptic function bandpass filters (BPFs) are presented, based on the concept of bandstop resonator (BSR) sections. One or more single-mode and multiple-mode BSRs can be dangled from a non-resonant node. Each BSR can generate one reflection zeroes (RZ) and one transmission zeroes (TZ). Multiple BSR sections are used to flexibly and independently control the location and bandwidth of the stop bands and therefore the same of the passbands. The method to design single- and multiple-band elliptic function BPFs has been detailed using a number of examples based on waveguide technology. For proof of concept, a 6th-order single-band BPF with six BSR = 2 sections and a 3$^{\text{rd}}$-order dual-band BPF using three BSR = 3 sections are designed and fabricated monolithically using a selective-laser-melting (SLM) 3-D printing technique. Excellent agreement between simulated and measured results verifies the proposed design methodology and its versatility as well as the additive-manufacture approach.

INDEX TERMS Bandpass filter, bandstop resonator, e-plane stubs, multiple bands, transmission zeroes, waveguide filter.

I. INTRODUCTION

Compared with Butterworth and Chebyshev responses, elliptic and quasi-elliptic bandpass filters (BPF) offer a better solution for the filtering structure because they can simultaneously synthesize in-band reflection zeroes (RZs) and out-of-band transmission zeroes (TZs). This leads to better in-band flatness, sharper roll-off at the band-edge, and higher out-of-band rejection. There are several well-established techniques that can be used to generate TZs. Firstly, creating more coupling paths can produce TZs. This can be achieved through cross-coupling between non-adjacent resonators [1], [2], [3], [4], or transversal topology based on multiple-mode resonators (MMRs) [5], [6]. Secondly, frequency-variant coupling [7], [8], [9], [10] may be used when the inverters J not only control the coupling between resonators, but also generate TZs. Thirdly, TZs can be generated by the resonator itself, which means that the resonators in a filter can be used to produce both RZs and TZs. There is also the TZ-generating bandstop resonator (BSR) [11], [12], [13], [14]. What is most interesting about this technique is its inherently low transmission loss in the passband when used to synthesize elliptic-function BPFs, since it resonates in the stopband rather than the passband. Extracted pole resonator [15], [16], [17] is also widely used to produce one RZ-TZ pair. It will become clear later that this can be treated as a special case of one BSR section (denoted as BSR = 1 in this work, as will be detailed later), while the dual-behavior resonator originally came from [18] and further developed in [19], [20], [21], can be treated as the case of two BSR sections (i.e., BSR = 2), producing two RZs and two TZs.

Multiple-band filters are in growing demand in new communication systems. A simple and effective method to design a multiple-band filter is the use of MMRs with their modes coinciding with the center frequencies of the specified passbands. Multiple-band filters can be realized in other ways: (1) Using transversal topology based on multiple-mode bandpass resonators (BPRs). Dual-band filters based on two BPR sections (denoted as BPR = 2) [22], [23], [24] and triple-band filters based on BPR = 3 sections [25], [26], [27] have been demonstrated using resonators of different unloaded quality factors. In [23], a dual-mode circular spiral resonator is adopted in a 2^{nd}-order dual-band filter with a miniaturized circuit size, with the TZs implemented by the source-load coupling. In [25], three fundamental modes (TE_{111V}, TM_{010}, and TE_{111H}) are excited and coupled simultaneously in a triple-band filter; (2) By the combined use of BPR and BSR in a resonator section. Dual-band filters based on BPR = 1 & BSR = 1 sections and triple-band filters based on BPR = 1 & BSR = 2 sections are synthesized and designed in [28] and [29]. Both methods can be used to control the multiple frequency bands individually. However, the number of realizable TZs is limited. In order to achieve more TZs, the cross-coupling technique was used in [23] and [28]. This inevitably increases the geometric complexity and model sensitivity to dimensional tolerance. [30] proposed a 250 GHz waveguide filter using two groups of E-plane stubs, which achieved 5th-order response with 5 TZs in lower stopband while 5 TZs in upper stopband.

In this paper, the design of multiband filters based on multiple BSR sections are proposed for the first time. It is based on the concept of dual-behavior resonators [18], [19], [20], [21], where the center RZ of two BSR sections forms a passband between the sets of TZs for single-band filter design. Compared with the conventional use of multiple BPRs in a section [31], [32], [33], the filters using multiple BSRs have lower insertion loss since the BSR resonates in the stopband avoiding excessive energy consumption associated with resonators in the passband. Furthermore, multiple BSRs in a section can be more easily implemented and independently controlled than multiple BPRs. This helps to reduce the design complexity. A 6th-order single-band filter based on BSR = 2 sections and a 3^{rd}-order dual-band filter based on BSR = 3 sections are designed, fabricated, and measured in this work. The key features of the proposed multiband filters are: (1) Elliptic-function response with up to $2 \times N$ TZs can be generated beside the passband in a N-*th*-order filter. (2) Low insertion loss, as the BSR sections resonate in the stopband rather than in the passband. (3) A cascaded configuration with low geometric complexity and therefore low susceptibility to manufacturing tolerance.

II. CIRCUIT ANALYSIS OF THE BSR SECTION

Fig. 1(a) presents the equivalent circuit of a composite bandpass-bandstop resonator section (RS). It composes m BPRs and n BSRs in a single section. The BPRs are connected in parallel to the source and load via inverters J_m, while the n BSRs are dangled in the same resonator section with their respective inverters J_n. There are a total of four cases to be discussed in a single RS: (1) BPR = 0 & BSR = 0, (2) BPR ≠ 0 & BSR = 0, (3) BPR = 0 & BSR ≠ 0, and (4) BPR ≠ 0 & BSR ≠ 0. This paper concerns the case with BPR = 0 & BSR ≠ 0 case, and a series of single-band and multiple-band BPFs will be synthesized based on this type of resonator section. Its equivalent circuit is shown in Fig. 1(b), which includes n BSRs and no BPR. The source and load conductances G_S and G_L are both normalized to unity. Each BSR is represented by the frequency-dependent unit capacitors $s = j\omega$ in parallel with the frequency-independent reactances (FIR) jB. Since there is no BPR, all BSRs are dangled in parallel on the main all-pass line with their respective inverter J_s. The interconnection node (non-resonating node) between the BSR and main line is represented by the junction reactance jB_{NRN}.

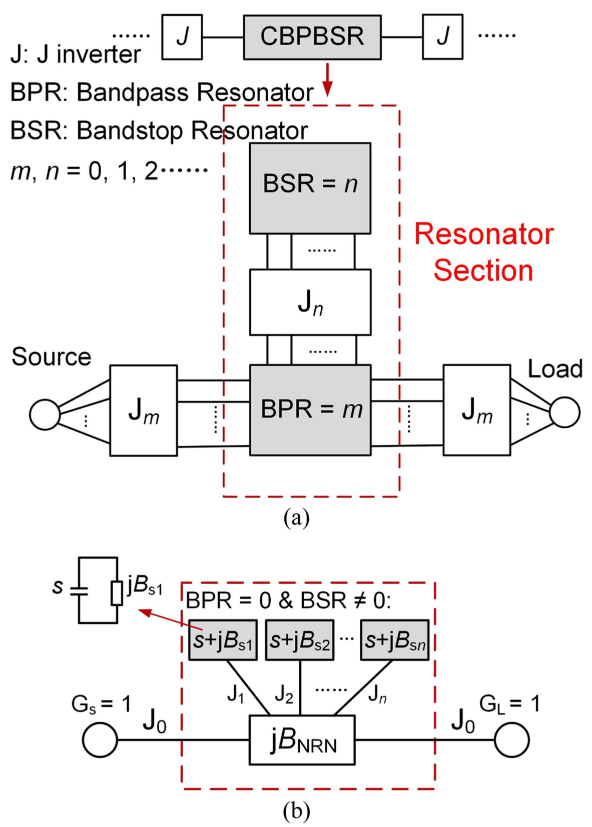

FIGURE 1. (a) Equivalent circuit of a generic composite bandpass-bandstop resonator (CBPBSR) section. (b) The case with BPR = 0 & BSR ≠ 0.

For each BSR, the input admittance $Y_{in,k}$ ($k = 1, 2, \ldots\ldots$) seen from their respective inverter J_{sk} to the resonator $s{+}jB_{s,k}$ can be expressed as

$$Y_{in,k}(s) = \frac{J_{s,k}^2}{s + jB_{s,k}}. \tag{1}$$

The input admittance Y_{inBSR} seen from the junction reactance jB_{NRN} to the n BSR admittances is given by

$$Y_{in\_BSR}(s) = jB_{NRN} + \sum_{k=1}^{n} Y_{in,k}(s). \tag{2}$$

The input admittance Y_{in} from the source can be obtained by

$$Y_{in}(s) = \frac{J_0^2}{Y_{in\_BSR} + J_0^2}, \tag{3}$$

where J_0 is the inverter between the source/load and the non-resonating node. Y_{in} is also related to the reflection coefficient by

$$Y_{in}(s) = \frac{1 - S_{11}(s)}{1 + S_{11}(s)}. \tag{4}$$

Therefore, the S-parameters of the n BSR sections can be derived as

$$S_{11}(\omega) = \frac{\prod_{k=1}^{n}\left(\omega + B_{sk} - \frac{J_{sk}^2}{B_{NRN}}\right)}{E_s(\omega)} \tag{5a}$$

$$S_{21}(\omega) = \frac{-2J_0^2 \prod_{k=1}^{n}(\omega + B_{sk})}{E_s(\omega)}, \tag{5b}$$

where $E_s(\omega)$ are the polynomial denominators of both $|S_{11}|$ and $|S_{21}|$ with the polynomials of degree n. It is deduced that the numerator of $|S_{21}|$ has n zeroes with $\omega_k = -B_{s,k}$ ($k = 1, \ldots, n$), while the numerator of $|S_{11}|$ also has n zeros.

The first three BSR sections (BPR = 0 & BSR = k, $k = 1, 2, 3$) will be investigated in the following sections. Single-band and multiple-band BPFs will be demonstrated. Waveguide technology will be adopted to implement the designs.

III. RESONATOR SECTION WITH BPR = 0 & BSR = 1

The equivalent circuit of a RS with BPR = 0 & BSR = 1 is shown in Fig. 2(a). It has an FIR named jB_{s1}, dangled on the main line via inverter J_{s1} and the junction reactance jB_{NRN}. According to (5), when $n = 1$, there is one zero at $\omega_{p1} = -B_{s1} + J_{s1}^2/B_{NRN}$ in $|S_{11}|$ and one zero at $\omega_{s1} = -B_{s1}$ in $|S_{21}|$. This RS model is essentially the well-known extracted pole resonator [15], [16], [17]. To implement the resonator section, an E-plane TM-mode waveguide resonator is dangled on the straight waveguide section via a coupling iris as shown in Fig. 2(b). The length a is equal to the broad wall width of the standard WR-28 waveguide, while the width b and height c are used to control the resonant frequency and unloaded quality factor (Q_u), respectively. The resonant frequencies of this waveguide resonator can be represented by

$$\omega_{(1,m,0)}{}^2 = \frac{v^2}{\varepsilon_r \mu_r}\left[\left(\frac{\pi}{a}\right)^2 + \left(\frac{m\pi}{b}\right)^2\right], \tag{6}$$

where v stands for the speed of light in the vacuum, ε_r and μ_r are the permittivity and permeability of the air, respectively.

The first three resonant modes in this waveguide resonator are TM_{110}, TM_{120}, and TM_{130}. Their resonant frequencies versus b and Q_u values versus c are shown in Fig. 2(c). It can be seen that TM_{110} has the lowest resonant frequency, followed by TM_{120} and TM_{130}. As b increases, the three modes shift to lower frequencies. The Q_u value decreases from TM_{130} to TM_{110} modes. When c increases, Q_u values of the three modes become larger. Fig. 2(d) presents the simulated S-parameters of the model in Fig. 2(b), where $a = 7.12$, $b = 8$, $c = 2$, $l = 1$, $w = 1$, all in millimeter (mm). As expected, there are three transmission zeroes (TZs) from 20 to 40 GHz. The TM_{110} TZ is at 21.9 GHz, while TM_{120} TZ at 27.5 GHz, and TM_{130} TZ at 37.8 GHz.

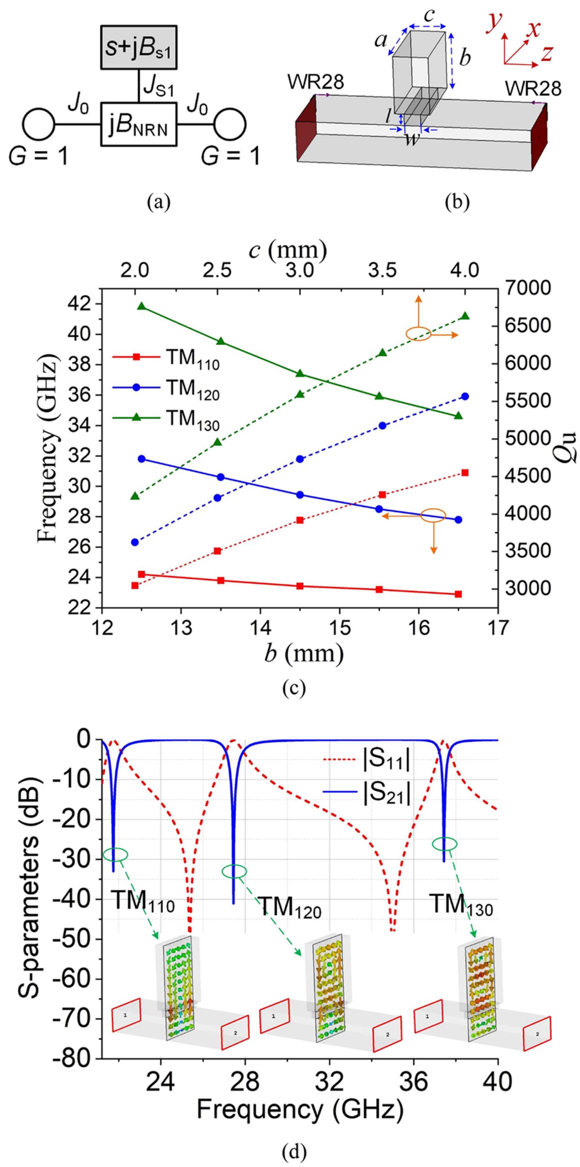

FIGURE 2. **RS with BPR = 0 & BSR = 1: (a) Equivalent circuit, (b) Waveguide model, (c) Frequencies and Q_u values versus varied parameters; (d) Simulated S-parameters of waveguide resonator.**

Fig. 3 presents a 5th-order waveguide bandstop filter prototype using BSR = 1 section E-plane stubs. In Fig. 3(a), five stubs are all placed on the same side of the waveguide with a separation of $1/4\lambda_0$ in between, where λ_0 is the wavelength of

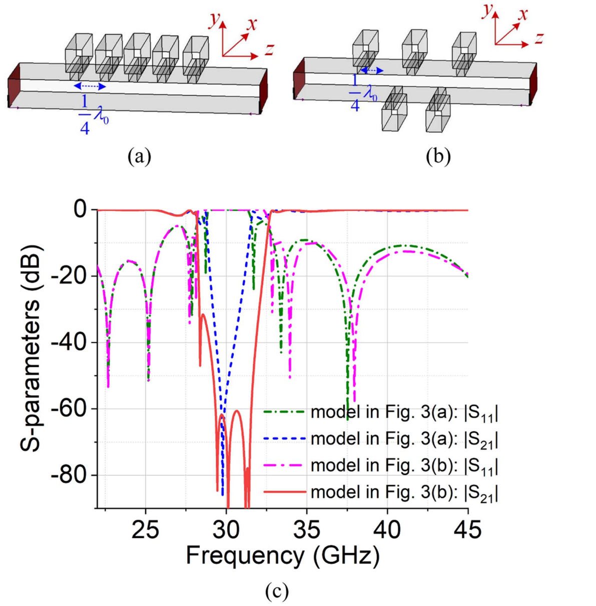

FIGURE 3. **A 5th-order bandstop filter with: (a) All stubs are on the same side, (b) Stubs are on the opposite side, (c) S-parameters.**

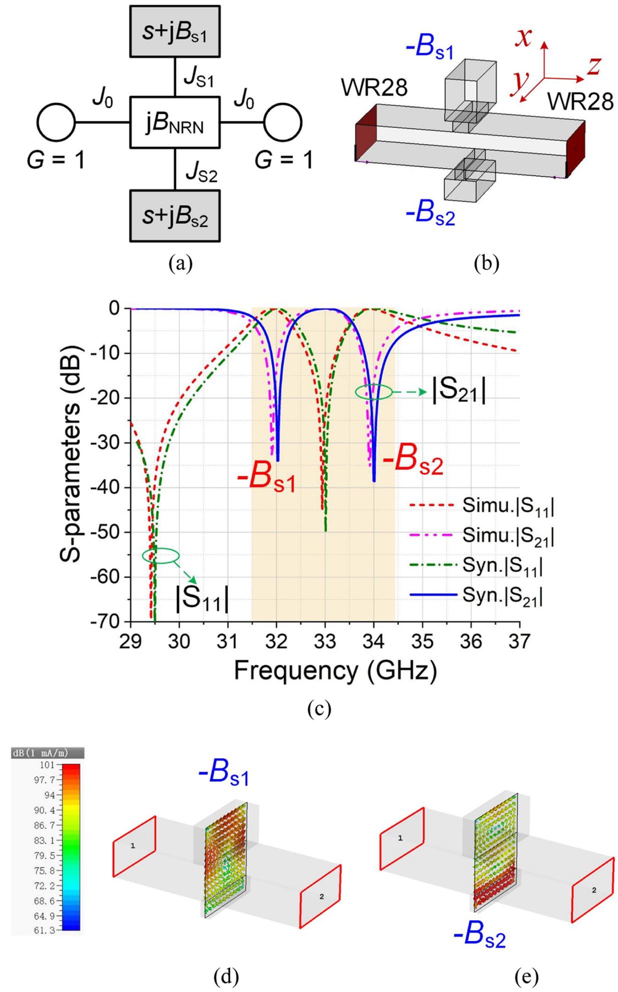

FIGURE 4. **RS with BPR = 0 & BSR = 2: (a) Equivalent circuit, (b) Waveguide model, (c) The synthesized and simulated S-parameter comparison (The orange area represents the utilized RZs and TZs), (d) H-field distribution at 32 GHz, (e) H-field distribution at 34 GHz.**

the center frequency in free space. In Fig. 3(b), the first, third, and fifth stubs are still on the same side, while the second and fourth stubs are placed on the opposite side of the waveguide. The distance between the alternating stubs is still 1/4 λ_0. The simulated S-parameters in Fig. 3(c) show that the alternating configuration in Fig. 3(b) has a wider bandwidth than that in Fig. 3(a). This feature could lead to a wider spurious-free bandwidth when used in a BPF design. Therefore, the configuration with alternating stubs will be adopted in the following designs.

IV. SINGLE-BAND ELLIPTIC-FUNCTION FILTER

This section presents the design of a single-band elliptic-function filter based on a RS with BPR = 0 & BSR = 2. We will first use a simple 1st-order filter to demonstrate the concept and design methodology. Its equivalent circuit is shown in Fig. 4(a), which includes two FIRs, jB_{s1} and jB_{s2}, dangled on the main line through inverters J_{s1} and J_{s2}. According to (5), when $n = 2$, both $|S_{11}|$ and $|S_{21}|$ have two zeroes:

$$\omega_{s1} = -B_{s1}, \omega_{s2} = -B_{s2} \tag{7a}$$

$$\omega_{p1} = -B_{s1} + \frac{J_{s1}^2}{B_{NRN}}, \omega_{p2} = -B_{s2} + \frac{J_{s2}^2}{B_{NRN}}, \tag{7b}$$

For a 33 GHz filter with a 10% fractional bandwidth (FBW), the external quality factor (Q_e) is determined by FBW and also calculated by $Q_e = B_{NRN}/J_0{}^2$ [16], the parameter values of equivalent circuit in Fig. 4(a) are obtained as follows: $B_{s1} = -1.2$, $B_{s2} = 1.2$, $B_{NRN} = -0.6$, $J_{s1} = 1.3$, $J_{s2} = 1$ and $J_0 = 1$. An E-plane waveguide model is used to realize the design as shown in Fig. 4(b). It has two E-plane TM_{110} mode stubs. The derived S-parameter responses from the resonator section using formulas (1)–(5) and the simulation is compared in Fig. 4(c). They are in very good agreement. One TZ is at 32 GHz and the other at 34 GHz, while one reflection zero (RZ) occurs between the two TZs at 33 GHz, and the other at 29.5 GHz. Fig. 4(d) and (e) present the simulated H-field distributions at the two TZs. A magnetic-field loop can be seen in both cases, indicating TM_{110} mode.

The 1st-order filter is of little practical use. Now we will apply the same method and design a 6th-order waveguide BPF at the center frequency of 33.4 GHz and with a FBW of 10.7%, a return loss better than 20 dB, and an out-of-band rejection higher than 40 dB (from 28 to 31 GHz and 36 to 44 GHz). The low-pass prototype circuit is shown in Fig. 5(a). It contains six cascaded resonant sections with BPR = 0 & BSR = 2. All the RSs are coupled using inverters. As shown in Fig. 5(b), it consists of two groups of E-plane stubs. The group of longer stubs will be responsible for defining the lower stopband, whereas the group of shorter stubs will define the upper stopband. Each group can be designed separately. An alternating stub configuration is used for each group as in the

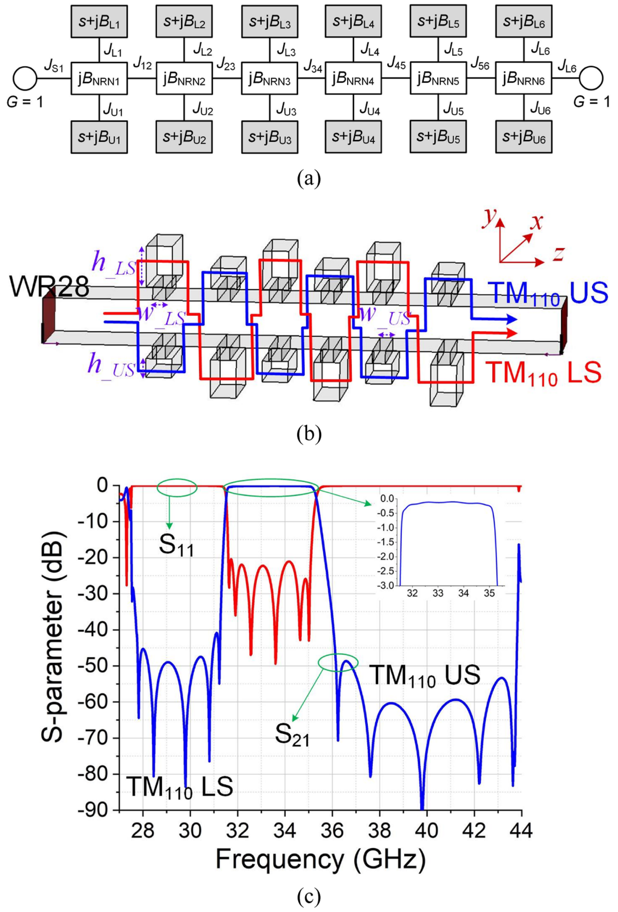

FIGURE 5. 6th-order waveguide BPF using RS with BPR = 0 & BSR = 2: (a) Low-pass prototype circuit, (b) Geometry, LS: low stopband, US: upper stopband, (c) Simulated S-parameters.

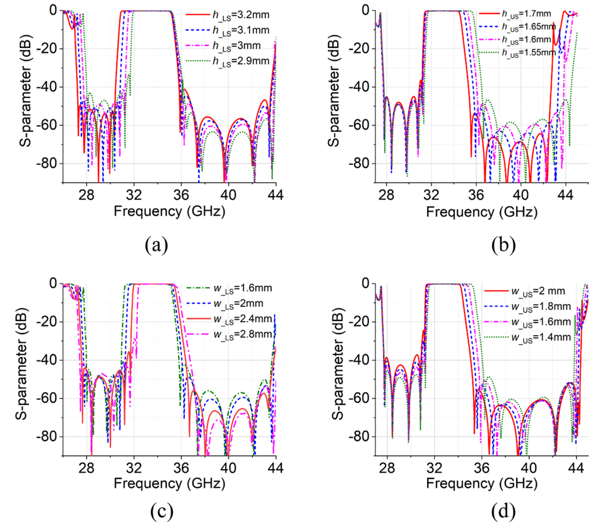

FIGURE 6. Parameter study for $|S_{21}|$ in the 6th-order single-band filter: (a) $h\__{LS}$, (b) $h\__{US}$, (c) $w\__{LS}$, (d) $w\__{US}$.

case of Fig. 3. The extracted Q_e of low stopband TM_{110} and upper stopband TM_{110} modes are 34.4 and 37.2, respectively. The simulated S-parameters are given in Fig. 5(c). It is evident that six TZs are realized in the lower stopband centered at 29.5 GHz with a 40 dB out-of-band rejection bandwidth of 3.3 GHz. For the upper stopband centered at 40 GHz, again six TZs are identifiable. The 40 dB rejection bandwidth is 6 GHz. The passband is clearly defined with six RZs and a return loss better than 20 dB. The minimum simulated insertion loss is 0.2 dB when brass material with a conductivity of 2.74×10^7 S/m is assumed. The 20 dB return-loss (RL) bandwidth is from 31.7 GHz to 35.3 GHz.

Fig. 6 presents the parameter study to show the independent control of the lower and upper passband edges. When $h\__{LS}$ decreases, the lower stopband shifts to the higher frequency maintaining a constant fractional stopband bandwidth, while the upper stopband remains unchanged. Similarly in Fig. 6(b), the smaller the $h\__{US}$ values are, the higher the upper stopband frequencies. $w\__{LS}$ and $w\__{US}$ can be used to control the stop bandwidth. When $w\__{LS}$ increases, the achieved lower stopband bandwidth is reduced, and it slightly affects the upper stopband. When $w\__{US}$ increases, the upper stopband bandwidth is reduced, and the lower stopband remains unchanged. Essentially, these four parameters can individually control the location and the bandwidth of both stopbands.

This 6th-order BPF was 3-D printed monolithically using a selective laser melting process by a Concept Laser M2 printer. More specifically, all prototypes in this work were printed monolithically using A20X alloy (aluminum-copper alloy). After printing, the flange interfaces were polished to ensure good interconnection with the test ports. The printed prototype is shown in Fig. 7(a), with a size of $19.1\times19.1\times40$ mm^3. Fig. 7(b) presents the internal physical dimensions of the air-filled stubs and waveguides. Fig. 7(c) compares the simulated S-parameters by CST studio and measured results. The measured $|S_{21}|$ curve is slightly shifted up by 100 MHz (2.7% passband bandwidth), but generally matches very well with the simulation. The measured minimum in-band insertion loss is 0.45 dB, compared with 0.2 dB in simulation, as shown in the inset of Fig. 7(c). The measured $|S_{11}|$ is below -12 dB, worse than the simulated one, which may be attributed to the printing tolerance and the high surface roughness, typically 5–7 μm.

V. DUAL-BAND ELLIPTIC-FUNCTION FILTER

This section will present the design of a dual-band filter based on a resonant section with BPR = 0 & BSR = 3, using a dual-mode resonator.

We first introduce the dual-mode resonator. Its geometry is shown in Figs. 8(a) and (b). It is still based on TM_{1m0} waveguide cavity where c is much smaller than a and b as in Fig. 2(b). A key feature is that a metal post is inserted into the cavity from the xoy plane. The post has a radius of r and a length of h. The E-field distributions of the first four modes (TM_{110}, TM_{120}, TM_{130}, and TM_{140}) are plotted in Fig. 8(c). Because the field of the TM_{120} and TM_{140} has a minimum at the position of the post, the post would only have a significant

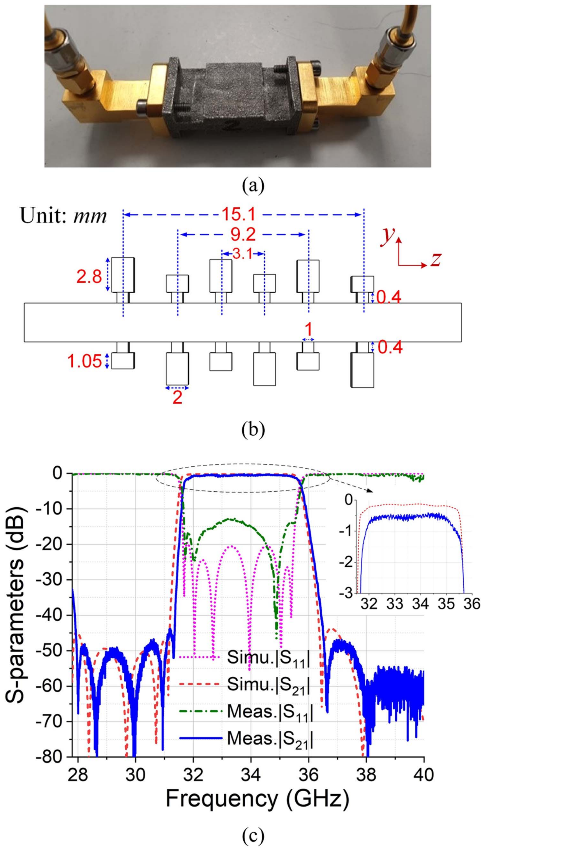

FIGURE 7. 6th-order BPF model with: (a) Photograph of the 3-D printed prototype, (b) Physical dimensions, all in *mm*, (c) simulated and measured S-parameters.

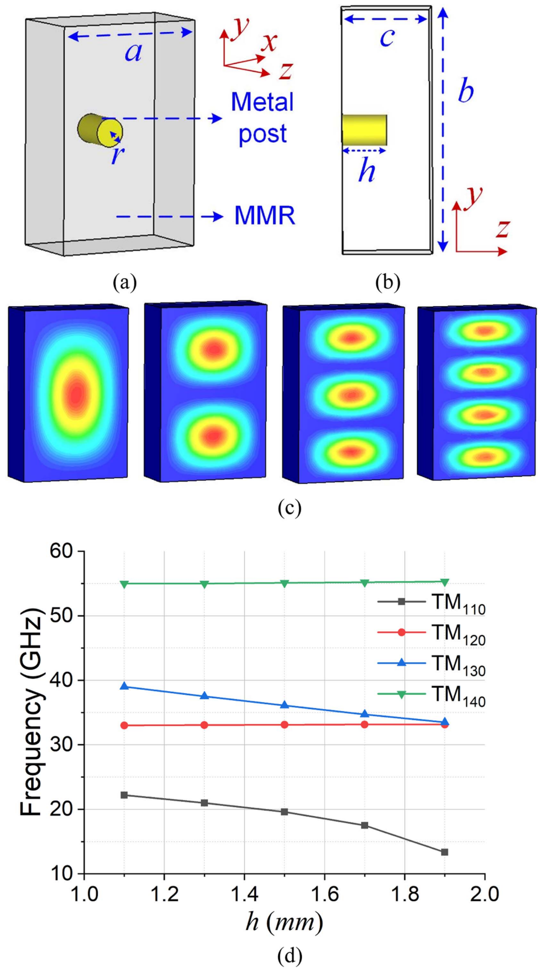

FIGURE 8. Waveguide resonator with metal post: (a) 3-D view, (b) *yoz* plane cross section, (c) E-field energy density of the first four modes, (d) Frequencies change versus post length *h*.

influence on the TM_{110} and TM_{130} modes. The parameter study in Fig. 8(d) shows that when h increases, the TM_{110} and TM_{130} shift to lower frequencies, while TM_{120} and TM_{140} remain unchanged. This property can be used to control the separation between the TM_{120} and the TM_{130}. We use this behavior of the two modes in the following designs to control the frequency ratio of the two bands.

The low-pass prototype circuit of the RS with BPR = 0 & BSR = 3 is shown in Fig. 9(a). It includes three FIRs jB_{s1}, jB_{s2}, and jB_{s3}. According to (5), when $N = 3$, both $|S_{11}|$ and $|S_{21}|$ have three zeroes:

$$\omega_{s1} = -B_{s1}, \omega_{s2} = -B_{s2}, \omega_{s3} = -B_{s3}, \tag{8a}$$

$$\omega_{p1} = -B_{s1} + \frac{J_{s1}^2}{B_{NRN}}, \omega_{p2} = -B_{s2} + \frac{J_{s2}^2}{B_{NRN}},$$
$$\omega_{p3} = -B_{s3} + \frac{J_{s3}^2}{B_{NRN}}, \tag{8b}$$

The center frequencies of the dual-band filter have been specified to be 30.5 GHz and 32.5 GHz with FBWs of 2% and 2%. The parameter values of equivalent circuit in Fig. 9(a) are obtained as follows: $B_{s1} = -2.5$, $B_{s2} = 0$, $B_{s3} = 2.55$, $B_{NRN} = -0.6$, $J_{s1} = 1.6$, $J_{s2} = 1.2$, $J_{s3} = 1.4$, and $J_0 = 1$. The waveguide model used to implement the RS is presented in Fig. 9(b). It has two E-plane stubs. One stub has an inserted metal post used to control the two resonant modes TM_{120} and $TM_{130,}$ corresponding to jB_{s1} and jB_{s3}. The other stub will operate as a single TM_{120} mode. The comparison in Fig. 9(c) shows good agreement between the synthesized and simulated S-parameters. There are three TZs at 29.5 GHz, 31.5 GHz, and 33.5 GHz. Two RZs are sandwiched between the three TZs, while the third at 24.4 GHz.

Now we will demonstrate a dual-band filter: 3$^{\text{rd}}$-order for each band, center frequencies at 30.5 GHz and 32.4 GHz, FBW of 2% and 2.2%, return loss better than 15 dB, and out-of-band rejection better than 30 dB (from 29 to 30 GHz, 31.1 to 31.7 GHz, 33.1 to 34 GHz). The low-pass prototype circuit is shown in Fig. 10(a). It has three cascaded RSs of BPR = 0 & BSR = 3. The waveguide model is shown in Fig. 10(b). It includes two groups of E-plane stubs following the alternating layout. The group of longer stubs with metal post support the two resonant modes (TM_{120} and TM_{130}). TM_{120} is responsible for the lower stopband (LS, as indicated in Fig. 10), whereas TM_{130} is for the upper stopband (US). The group

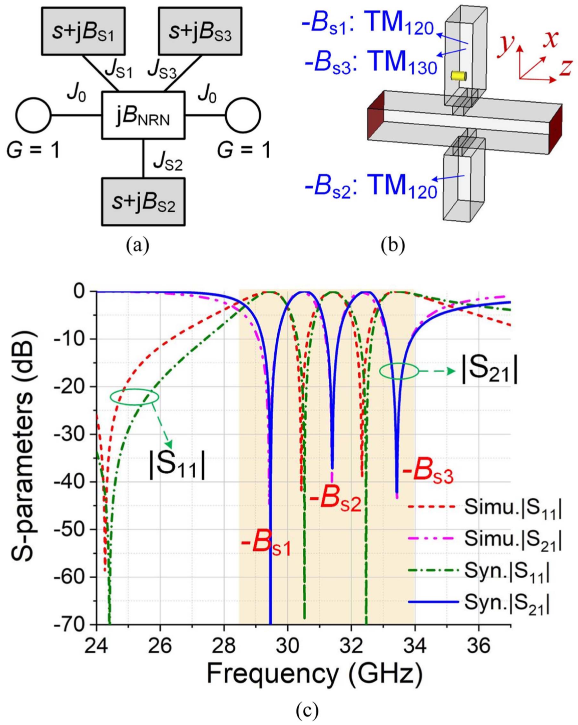

FIGURE 9. RS with BPR = 0 & BSR = 3: (a) Equivalent circuit, (b) Waveguide model, (c) The synthesized and simulated S-parameter comparison (The orange area represents the utilized RZs and TZs).

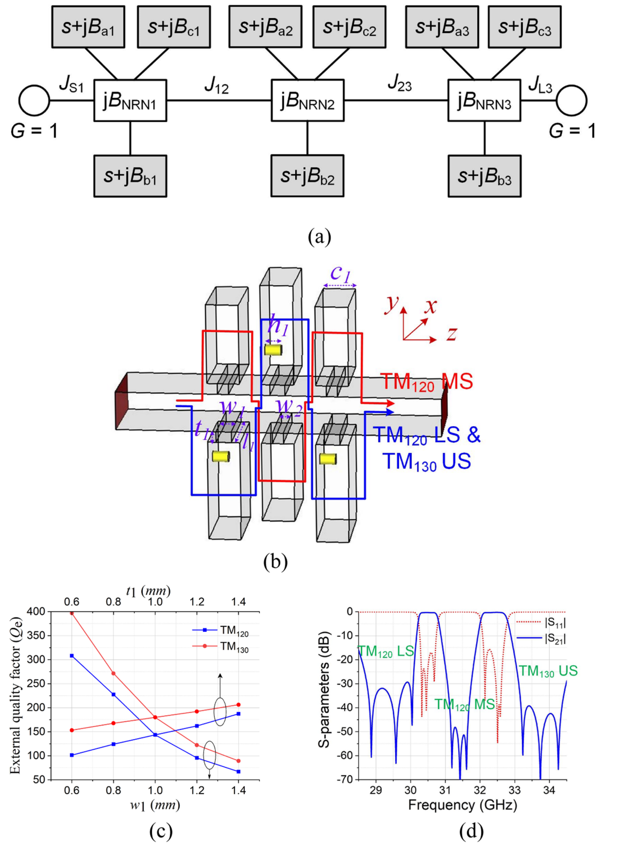

FIGURE 10. 3rd-order dual-band waveguide BPF using RS with BPR = 0 & BSR = 3: (a) Low-pass prototype circuit, (b) Geometry, LS: low stopband, MS: middle stopband, US: upper stopband, (c) Extracted external quality factor (Q_e) curves of TM_{120} and TM_{130} in a dual-mode resonator, (d) Simulated S-parameters.

of shorter stubs (with no post) supports a TM_{120} resonant mode at the middle stopband (MS). Therefore, each of the RS contributes to the three stopbands that separate the two passbands. Since the slot between mainline and dual-mode BSR controls the Q_e values of TM_{120} and TM_{130} modes in the dual-mode resonator [21], Fig. 10(c) presents the Q_e curves of TM_{120} and TM_{130} versus width w_1 and thickness t_1 change. The extracted Q_e values of TM_{120} (LS), TM_{130} (US) in the dual-mode resonator and TM_{120} (MS) in the single-mode resonator are 143.5, 180, and 157.7, respectively. The simulated S-parameters are shown in Fig. 10(d). Each stopband has three transmission zeros. Each passband has 3 RZs with a return loss better than 17 dB. The minimum insertion loss of the lower band is 0.3 dB, and the 1-dB bandwidth is from 30.2 GHz to 30.8 GHz, while the upper passband has a minimum insertion loss of 0.2 dB and 1-dB bandwidth from 32.1 GHz to 32.8 GHz.

Fig. 11 uses the parameter study to show the independent control of the stopbands/passbands. In addition to the width b of the waveguide resonator controlling the resonant frequencies of TM-type modes as shown earlier in Fig. 2(c), the width of the coupling slot between waveguide resonator and the main line also affects the frequencies of these modes. As shown in Fig. 11(a), when the width w_1 of the slots between the dual-mode resonator and the main line increases, both LS and US shift to higher frequencies, where LS shows a lager frequency offset. In Fig. 11(b), when the width w_2 of the slots between the TM_{120} resonator and the main line increases, MS move to higher frequency, while LS and US remain unchanged. The height c_1 of the shorter stubs control the Q_u value of the resonator and the frequency ratio of the two passbands. As it increases, the MS moves to a lower frequency, and the fractional bandwidth increases from 2.5% to 3%, as plotted in Fig. 11(c). The length h_1 of the metal post in the longer stubs is used to independently control the US frequency. As shown in Fig. 11(d), US moves to a lower frequency when h_1 increases.

The same printer was used to manufacture the monolithic dual-band filter (Fig. 12(a)), including the metal posts that would be tricky to implement otherwise. However, the printing tolerance (100-200 μm) has a more significant adverse effect on the complex internal structure. Although the measured S-parameters generally match well with the simulation especially across the three stopbands, the measured insertion losses are higher than expected at 1.3 dB and 1.2 dB for the two passbands, and the passband matching degrades significantly as shown in Fig. 12(c). A higher precision printer may be required to print complex structures like the posts at this high frequency and a better solution to polish and refine the internal cavities of the monolithic 3-D print structures.

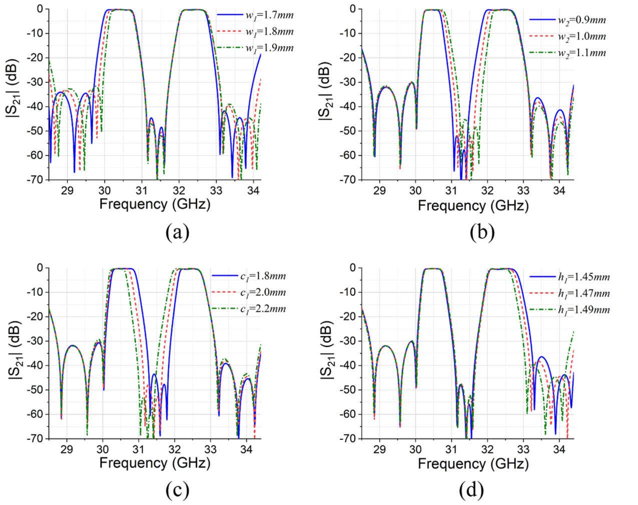

FIGURE 11. Parameter study for $|S_{21}|$ in the dual-band filter: (a) w_1, (b) w_2, (c) c_1, (d) h_1.

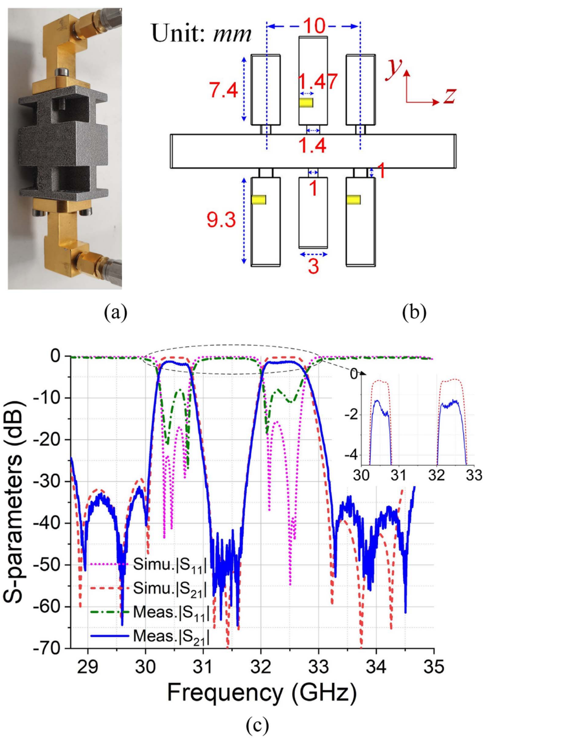

FIGURE 12. 3[rd]-order dual-band BPF model with: (a) Photograph of the 3-D printed prototype, (b) Physical dimensions, all in *mm*, (c) simulated and measured S-parameters.

The internal physical parameter dimensions are shown in Fig. 12(b).

Furthermore, a triple-band filter using RSs with BPR = 0 & BSR = 4 is designed as single section shown in Fig. 13(a)–(b). Then, three RSs with BPR = 0 & BSR = 4 are cascaded to form 3[rd]-order triple-band BPF as low-pass prototype circuit and waveguide model shown in Fig. 13(c)–(d). The group of longer stubs with metal posts propagates TM_{120} low stopband (LS) and TM_{130} middle-upper stopband (MUS) modes, while the group of shorter stubs with the metal posts propagates TM_{120} middle-low stopband (MLS) and TM_{130} upper stopband (US) modes. The simulated S-parameters are provided in Fig. 13(e), which shows four prescribed stopbands. Three passbands, each of a 3[rd]-order response, are sandwiched between the stopbands.

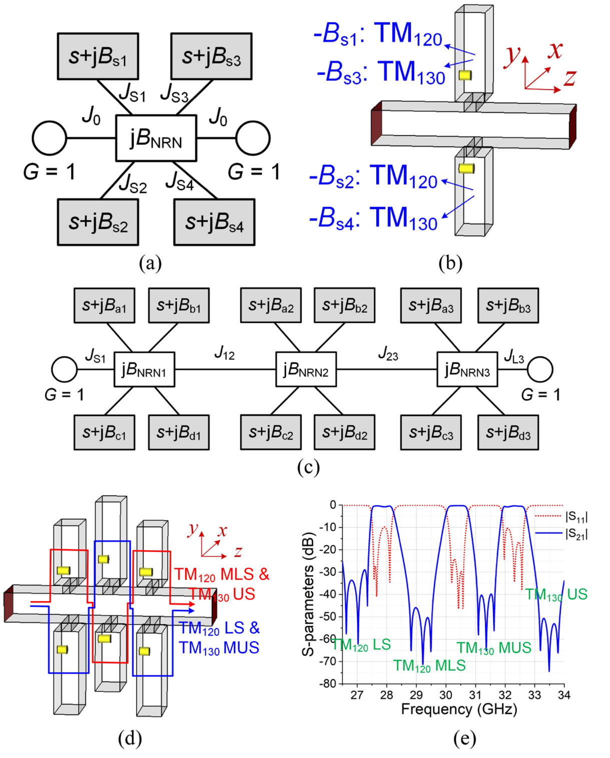

FIGURE 13. RS with BPR = 0 & BSR = 4: (a) Equivalent circuit, (b) Waveguide model, and 3[rd]-order triple-band waveguide BPF using RS with BPR = 0 & BSR = 4: (c) Low-pass prototype circuit, (d) Geometry, LS: low stopband, MLS: middle-low stopband, MUS: middle-upper stopband, US: upper stopband, (e) Simulated S-parameters.

Finally, we summarize and compare the demonstrated waveguide multiple-band filters in this work with other reported ones in the literature in Table 1. Conventionally, multiple-mode bandpass resonators are usually adopted to implement multiple-band filter designs, i.e., dual-mode bandpass resonators [23], [24] for dual-band filters, triple-mode bandpass resonators [25], [26] for triple-band filters. In [28] and [29], the composite section with bandpass resonators and bandstop resonators were proposed for multiband filter designs (corresponding to a RS with BPR = 1 & BSR = 1 for dual-band filters, and a RS with BPR = 1 & BSR = 2 for triple-band filters). In this paper, we put forward a new single- and multiband filter design methodology, based on all BSR-based resonators. RSs with BPR = 0 & BSR = 2 for the single-band filter and RSs with BPR = 0 & BSR = 3 for the dual-band filter are designed and analyzed. Compared with the conventional methods, the proposed method has the merits of low insertion loss, up to $2\times N$ TZ generation in a N-th-order filter, and a cascaded configuration with low geometric complexity.

TABLE 1 Comparison With Reported Waveguide Multiple-Band Bandpass Filters

Ref.	Frequency (GHz)	FBW (%)	IL (dB)	Filtering Order	No. of TZs	Techniques	Type of resonator section
[23]-dualband	0.194/0.268	1.6/2.1	1.75/1.1	2/2	1/2/1	CNC	BPR = 2 & BSR = 0
[24]-dualband	3.44/3.57	1/1	0.15/0.22	4/4	1/2/1	CNC	BPR = 2 & BSR = 0
[28]-dualband	20/21	1.5/1.4	1.37/1.1	3/3	0/1/0	SIW	BPR = 1 & BSR = 1
[29]-dualband	3.7/4.2	8.1/4.3	0.26/0.3	2/2	0/1/0	3-D printing	BPR = 1 & BSR = 1
[25]-tripleband	3.8/4/4.2	1/0.9/0.8	0.22/0.22/0.22	4/4/4	0/1/1/0	CNC	BPR = 3 & BSR = 0
[26]-tripleband	2.95/2.99/3.03	0.3/0.2/0.2	0.6/1.7/1.2-	2/2/2	0/1/1/0	CNC	BPR = 3 & BSR = 0
[28]-tripleband	20/21/22	1.5/1.4/1.3	1.6/0.9/0.85	3/3/3	0/1/1/0	SIW	BPR = 1 & BSR = 2
[28]-tripleband	3.5/3.7/4.0	4.6/2.7/5.5	0.44/0.49/0.54	2/2/2	0/1/1/0	3-D printing	BPR = 1 & BSR = 2
Single-band	**33.4**	**10.7**	**0.4**	**6**	**6/6**	**3-D metal printing**	**BPR = 0 & BSR = 2**
Dual-band	**30.5/32.4**	**2/2.2**	**1.2/1.3**	**3/3**	**3/3/3**		**BPR = 0 & BSR = 3**

* FBW: 3-dB Fractional Bandwidth, IL: Minimum Insertion Loss, No. of TZs: Number of Transmission zeroes, CNC: Computer Numerical Control.
The bold values indicate the best performance.

VI. CONCLUSION

The key contribution of this work is the proposed multiple-band design concept and implementation method by exclusively using bandstop resonator sections. To validate this concept, multiple filter prototypes have been developed and tested, including a 6th-order single-band BPF and a 3rd-order dual-band BPF. The limitation of proposed BSR-based configuration lies in its relatively narrow spurious bands on both sides of the passband. Therefore, the use of BPR sections (which provides far-band suppression) and BSR sections (which provides near-band rejection) can be combined to synthesize the filter with wide spurious-free range. SLM-based 3D printing has been used to manufacture the filters in one piece without requiring any assembly. This also allows the monolithic manufacture of the metal posts inside the waveguide cavity. The approach reported in this work represents a new systematic design and implementation method to realize complex transfer functions by flexibly controlling the transmission zeros for single-band and multiple-band compact BPFs.

REFERENCES

[1] R. J. Cameron, “General coupling matrix synthesis methods for Chebyshev filtering functions,” *IEEE Trans. Microw. Theory Techn.*, vol. 47, no. 4, pp. 433–442, Apr. 1999.
[2] Y. Wang and M. Yu, “True inline cross-coupled coaxial cavity filters,” *IEEE Trans. Microw. Theory Techn.*, vol. 57, no. 12, pp. 2958–2965, Dec. 2009.
[3] S. Bastioli, R. Snyder, C. Tomassoni, and V. de la Rubia, “Direct-coupled TE–TM waveguide cavities,” *IEEE Microw. Wireless Technol. Lett.*, vol. 33, no. 6, pp. 819–822, Jun. 2023.
[4] S. Bastioli, R. V. Snyder, C. Tomassoni, and V. d. l. Rubia, “Direct-coupled TE–TM waveguide filters,” *IEEE Trans. Microw. Theory Techn.*, early access, Sep. 15, 2023, doi: 10.1109/TMTT.2023.3311960.
[5] D. R. Hendry and A. M. Abbosh, “Compact high-isolation base-station duplexer using triple-mode ceramic cavities,” *IEEE Trans. Ind. Electron.*, vol. 65, no. 10, pp. 8092–8100, Oct. 2018.
[6] S.-W. Wong et al., “Cavity balanced and unbalanced diplexer based on triple-mode resonator,” *IEEE Trans. Ind. Electron.*, vol. 67, no. 6, pp. 4969–4979, Jun. 2020.
[7] S. Amari and J. Bornemann, “Using frequency-dependent coupling to generate finite attenuation poles in direct-coupled resonator bandpass filters,” *IEEE Microw. Guided Wave. Lett.*, vol. 9, no. 10, pp. 404–406, Oct. 1999.
[8] Y. He et al., “A direct matrix synthesis for in-line filters with transmission zeros generated by frequency-variant couplings,” *IEEE Trans. Microw. Theory Techn.*, vol. 66, no. 4, pp. 1780–1789, Apr. 2018.
[9] G. Macchiarella, G. Gentili, and L. Accatino, “Stopband singlet: A novel structure implementing resonating couplings,” *IEEE Microw. Wireless Compon. Lett.*, vol. 30, no. 5, pp. 473–476, May 2020.
[10] E. López-Oliver, C. Tomassoni, G. Macchiarella, and M. Oldoni, “A frequency-variant coupling structure for inline rectangular waveguide filters,” in *Proc. IEEE/MTT-S Int. Microw. Symp. (IMS)*, 2023, pp. 533–536.
[11] H. Uchida et al., “Dual-band-rejection filter for distortion reduction in RF transmitters,” *IEEE Trans. Microw. Theory Techn.*, vol. 52, no. 11, pp. 2550–2556, Nov. 2004.
[12] J. D. Rhodes, “Waveguide bandstop elliptic function filters,” *IEEE Trans. Microw. Theory Techn.*, vol. 20, no. 11, pp. 715–718, Nov. 1972.
[13] J. R. Montejo-Garai, J. A. Ruiz-Cruz, J. M. Rebollar, and T. Estrada, “In-line pure E-plane waveguide band-stop filter with wide spurious-free response,” *IEEE Microw. Wireless Compon. Lett.*, vol. 21, no. 4, pp. 209–211, Apr. 2011.
[14] J. F. V. Sullca, S. Cogollos, V. E. Boria, M. Guglielmi, S. Bastioli, and R. Snyder, “Design of dual stopband filters for interference suppression,” in *Proc. IEEE/MTT-S Int. Microw. Symp. (IMS)*, 2023, pp. 525–528.
[15] J. D. Rhodes and R. J. Cameron, “General extracted pole synthesis technique with applications to low-loss TE/sub011/mode filters,” *IEEE Trans. Microw. Theory Techn.*, vol. 28, no. 9, pp. 1018–1028, Sep. 1980.
[16] O. Glubokov and D. Budimir, “Extraction of generalized coupling coefficients for inline extracted pole filters with nonresonating nodes,” *IEEE Trans. Microw. Theory Techn.*, vol. 59, no. 12, pp. 3023–3029, Dec. 2011.
[17] Y. Yang, M. Yu, and Q. Wu, “Advanced synthesis technique for unified extracted pole filters,” *IEEE Trans. Microw. Theory Techn.*, vol. 64, no. 12, pp. 4463–4472, Dec. 2016.
[18] C. Quendo, E. Rius, and C. Person, “Narrow bandpass filters using dual-behavior resonators,” *IEEE Trans. Microw. Theory Techn.*, vol. 51, no. 3, pp. 734–743, Mar. 2003.
[19] C. Quendo, E. Rius, and C. Person, “Narrow bandpass filters using dual-behavior resonators based on stepped-impedance stubs and different-length stubs,” *IEEE Trans. Microw. Theory Techn.*, vol. 52, no. 3, pp. 1034–1044, Mar. 2004.

[20] A. Manchec, C. Quendo, J.. -F. Favennec, E. Rius, and C. Person, "Synthesis of capacitive-coupled dual-behavior resonator (CCDBR) filters," *IEEE Trans. Microw. Theory Techn.*, vol. 54, no. 6, pp. 2346–2355, Jun. 2006.
[21] Q. Xue and J. Y. Jin, "Bandpass filters designed by transmission zero resonator pairs with proximity coupling," *IEEE Trans. Microw. Theory Techn.*, vol. 65, no. 11, pp. 4103–4110, Nov. 2017.
[22] W. S. Tang, S. Y. Zheng, Y. M. Pan, and H. W. Liu, "A frequency independently tunable dual-band bandpass filter with large frequency ratio and ultra-wide stopband," *IEEE Trans. Ind. Electron.*, vol. 70, no. 2, pp. 1894–1904, Feb. 2023.
[23] R. - S. Chen et al., "Miniaturized full-metal dual-band filter using dual-mode circular spiral resonators," *IEEE Microw. Wireless Compon. Lett.*, vol. 30, no. 6, pp. 573–576, Jun. 2020.
[24] L. Zhu, R. Mansour, and M. Yu, "Quasi-elliptic waveguide dual-band bandpass filters," *IEEE Trans. Microw. Theory Techn.*, vol. 67, no. 12, pp. 5028–5037, Dec. 2019.
[25] L. Zhu, R. Mansour, and M. Yu, "Triple-band cavity bandpass filters," *IEEE Trans. Microw. Theory Techn.*, vol. 66, no. 9, pp. 4057–4069, Sep. 2018.
[26] S. W. Wong, Z. C. Guo, J. Y. Lin, L. Zhu, and Q. Zhang, "Triple-mode and triple-band cavity bandpass filter on triplet topology with controllable transmission zeros," *IEEE Access*, vol. 6, pp. 29452–29459, 2018.
[27] R. S. Chen et al., "Reconfigurable cavity bandpass filters using fluid dielectric," *IEEE Trans. Ind. Electron.*, vol. 68, no. 9, pp. 8603–8614, Sep. 2021.
[28] X. - P. Chen, K. Wu, and Z. - L. Li, "Dual-band and triple-band substrate integrated waveguide filters with Chebyshev and quasi-elliptic responses," *IEEE Trans. Microw. Theory Techn.*, vol. 55, no. 12, pp. 2569–2578, Dec. 2007.
[29] K. Zhao and D. Psychogiou, "Monolithic multiband coaxial resonator-based bandpass filter using stereolithography apparatus (SLA) manufacturing," *IEEE Trans. Microw. Theory Techn.*, vol. 70, no. 9, pp. 4156–4166, Sep. 2022.
[30] J. Y. Lin, Y. Yang, T. Zhang, and S. W. Wong, "A 250 GHz low-loss inline waveguide bandpass filter using bandstop resonator pairs," in *Proc. IEEE/MTT-S Int. Microw. Symp. (IMS)*, 2023, pp. 545–548.
[31] X. Q. Lin, J. Y. Jin, J. W. Yu, Y. Jiang, Y. Fan, and Q. Xue, "Design and analysis of EMIT filter and diplexer," *IEEE Trans. Ind. Electron.*, vol. 64, no. 4, pp. 3059–3066, Apr. 2017.
[32] D. R. Hendry and A. M. Abbosh, "Triple-mode ceramic cavity filters with wide spurious-free performance," *IEEE Trans. Microw. Theory Techn.*, vol. 65, no. 10, pp. 3780–3788, Oct. 2017.
[33] J. Y. Lin, S. W. Wong, Y. M. Wu, Y. Yang, L. Zhu, and Y. He, "Three-way multiple-mode cavity filtering crossover for narrowband and broadband applications," *IEEE Trans. Microw. Theory Techn.*, vol. 67, no. 3, pp. 896–905, Mar. 2019.